First detection of NHD and ND2 in the interstellar medium

M. Melosso, L. Bizzocchi, O. Sipilä, B. Giuliano, L. Dore, F. Tamassia, M.-A. Martin-Drumel, O. Pirali, E. Redaelli, P. Caselli

First detection of NHD and ND_2 in the interstellar medium

Amidogen deuteration in IRAS 16293–2422

M. Melosso[1], L. Bizzocchi[2], O. Sipilä[2], B. M. Giuliano[2], L. Dore[1], F. Tamassia[3], M.-A. Martin-Drumel[4], O. Pirali[4,5], E. Redaelli[2], and P. Caselli[2]

[1] Dipartimento di Chimica "Giacomo Ciamician", Università di Bologna, via F. Selmi 2, 40126 Bologna (Italy)
e-mail: mattia.melosso2@unibo.it
[2] Center for Astrochemical Studies, Max-Planck-Institut für extraterrestrische Physik, Gießenbachstraße 1, 85748 Garching (Germany)
e-mail: bizzocchi@mpe.mpg.de
[3] Dipartimento di Chimica Industriale "Toso Montanari", Università di Bologna, viale del Risorgimento 4, 40136 Bologna (Italy)
[4] Université Paris-Saclay, CNRS, Institut des Sciences Moléculaires d'Orsay, 91405 Orsay Cedex (France)
[5] SOLEIL Synchrotron, AILES beamline, l'Orme des Merisiers, Saint-Aubin, 91190 Gif-sur-Yvette (France)

ABSTRACT

Context. Deuterium fractionation processes in the interstellar medium (ISM) have been shown to be highly efficient in the family of nitrogen hydrides. To date, observations were limited to ammonia (NH_2D, NHD_2, ND_3) and imidogen radical (ND) isotopologues.
Aims. We want to explore the high frequency windows offered by the *Herschel Space Observatory* to search for deuterated forms of amidogen radical NH_2 and to compare the observations against the predictions of our comprehensive gas-grain chemical model.
Methods. Making use of the new molecular spectroscopy data recently obtained at high frequencies for NHD and ND_2, both isotopologues have been searched for in the spectral survey towards the class 0 IRAS 16293-2422, a source in which NH_3, NH and their deuterated variants have been previously detected. We used the observations carried out with HIFI (Heterodyne Instrument for the Far Infrared) in the framework of the key program "Chemical *Herschel* surveys of star forming regions" (CHESS).
Results. We report the first detection of interstellar NHD and ND_2. Both species are observed in absorption against the continuum of the protostar. From the analysis of their hyperfine structure, accurate excitation temperature and column density values have been determined. The latter were combined with the column density of the parent species NH_2 to derive the deuterium fractionation in amidogen. Our findings point out a high deuteration level of amidogen radical in IRAS 16293-2422, with a deuterium enhancement about one order of magnitude higher than that predicted by earlier astrochemical models. Such a high enhancement can only be reproduced by a gas-grain chemical model if the pre-stellar phase preceding the formation of the protostellar system lasts long, of the order of one million years.
Conclusions. The amidogen D/H ratio measured in the low-mass protostar IRAS 16293-2422 is comparable to the one derived for the related species imidogen and much higher than that observed for ammonia. Additional observations of these species will give more insights into the mechanism of ammonia formation and deuteration in the ISM. We finally indicate the current possibilities to further explore these species at submillimeter wavelengths.

Key words. Astrochemistry – ISM: molecules – Line:identification – ISM: abundances – Submillimeter: ISM

1. Introduction

Despite the low cosmic abundance of deuterium (D/H = 1.5×10^{-5}, Linsky 2003), deuterated molecules can be found in the interstellar medium (ISM) with enormously large amounts and are routinely used as proxies for the cold environments typical of the early stages of the star formation process. It is well known that deuterium fractionation processes, *i.e.*, the deuterium enrichment in a given molecular species, can occur at very high rate under some specific physical conditions including, above all, a low gas temperature (5–20 K) and strong CO depletion (Caselli & Ceccarelli 2012). Inheriting such conditions from their pre-stellar core phase, Class 0 protostars are the astronomical objects which exhibit the largest molecular deuteration found so far (Ceccarelli et al. 2014). In the last few decades, several deuterium-bearing species (including doubly- and triply-deuterated forms) have been detected in these sources, e.g., water D_2O (Butner et al. 2007), formaldehyde D_2CO (Ceccarelli et al. 1998), hydrogen sulfide D_2S (Vastel et al. 2003), methanol CD_3OH (Parise et al. 2004), and ammonia ND_3 (Roueff et al. 2005; van der Tak et al. 2002).

The Class 0 protostar IRAS 16293-2422, located in the nearby ρ-Ophiuchi star-forming region (at a distance of ~120 pc), is considered a specimen for super-deuteration phenomena (Ceccarelli et al. 2007). Indeed, besides an exceptionally rich chemistry in its inner and warmer regions (van Dishoeck et al. 1995; Jørgensen et al. 2012; Fayolle et al. 2017), this source harbors a large number of interstellar deuterated species in the outer and cold envelope (Loinard et al. 2001). Among them, the family of neutral nitrogen hydrides (NH, NH_2, and NH_3) is well-represented, given that all the deuterated forms of ammonia (NH_2D, NHD_2, and ND_3) and the imidogen radical ND (Bacmann et al. 2010, 2016) have been detected so far. However, deuterium enrichment has never been observed for the amidogen radical NH_2, neither in IRAS 16293-2422 nor in any other astronomical sources.

Several factors may be imputed to the current lack of observation of interstellar NHD and ND_2. Until recently, laboratory data were limited to the frequency region below 500 GHz (Kanada et al. 1991; Kobayashi et al. 1997). At low temperatures, neither species possess any bright transitions in this portion of the spectrum, with *b*-type fundamental transitions lying high into the submillimeter-wave domain (around 770 GHz for NHD and around 527 GHz for ND_2). Furthermore, the amidogen radical is a textbook floppy molecule, for which frequency extrapolation from low frequency measurements is extremely unreliable. Besides the deficiency of laboratory spectral data, ground-based astronomical observations of these light species are hindered by the atmosphere opacity at submillimeter-wavelength. Therefore, even with high-frequency facilities (such as ALMA or SOFIA), the observation of light hydrides remains a challenging task. On-board observations using the *Herschel Space Observatory* mission, during which numerous projects attempted at gaining more insights into the chemistry of the ISM, offer a unique chance to overcome the latter issue. Also, now that recent laboratory studies of nitrogen hydrides in their various deuterated forms have been reported up to the terahertz domain (Melosso et al. 2017, 2019a,b, 2020; Bizzocchi et al. 2020), confident searches for these species can be undertaken in *Herschel* archival surveys.

In this paper, we report the first detection of NHD and ND_2 in the interstellar medium, thanks to HIFI[1] observations carried out as part of the CHESS[2] key program (PI: C. Ceccarelli). Both species were observed in absorption against the continuum of the low-luminosity protostar IRAS 16293-2422. From the modeling of their hyperfine structures, column densities of NHD and ND_2 have been determined and the deuterium fractionation of amidogen radical evaluated.

2. Observations

The observations analysed in the present paper have been retrieved from the HSA[3]. They were collected as part of CHESS key program, whose observational details have been given extensively in Ceccarelli et al. (2010). Briefly, the Class 0 protostar IRAS 16293-2422 was observed in March 2010 with the HIFI spectrometer (de Graauw et al. 2010; Roelfsema et al. 2012) for a total of 50 h. The targeted coordinates were $\alpha_{2000} = 16^{\rm h}23^{\rm m}22.75^{\rm s}$, $\delta_{2000} = -24°28'34.2''$. Seven different HIFI bands were employed to perform a spectral survey covering the frequency range between 480 and 1902 GHz almost continuously. The observations were carried out in double-sideband (DSB) using the wide band spectrometer (WBS), whose resolution is ~ 1.1 MHz.

For the present study we have employed bands 1a (488–552 GHz), 2b (724–792 GHz), and 4a (967–1 042 GHz), corresponding to the IDs number 1342191499, 1342192332, and 1342191619, respectively. HSA provides level 2.5 data products obtained with HIFI pipeline of the *Herschel* interactive processing environment (HIPE, Ott 2010). These data generally offer a scientific quality sufficient to perform the line analysis. However, given the weakness of the NHD and ND_2 spectral signals, we have also gone through the final processing manually. Starting from level 2 products, we have inspected all the data, manually removed bad scans, and exported all the "good" 1 GHz chunks to CLASS/GILDAS[4] format.

Side-band deconvolution has been performed with the minimization algorithm of Comito & Schilke (2002) implemented into CLASS90, and the resulting spectra have been cross-checked with the original level 2.5 products. In a few instances, the deconvolution procedure produced a small increase of the noise level compared to the averaged level 2 scans. In such cases, we directly use the DSB spectra after verifying that no interfering emission was present in the image band. At the later stage, intensive baseline subtraction on H- and V-polarisation spectra has been applied in the vicinity of each target feature; then, the two set of data have been re-sampled and averaged to obtain the final spectrum.

3. Analysis

The presence of amidogen radical in IRAS 16293-2422 has already been established by Hily-Blant et al. (2010), during the early phase of the CHESS key program. The results obtained in the previous study for the parent species NH_2 have been used to test the validity of our data processing and the subsequent spectral analysis. Figure 1 shows the strongest $J = \frac{3}{2} - \frac{1}{2}$ component of the fundamental $N_{Ka,Kc} = 1_{1,1} - 0_{0,0}$ transition of *o*-NH_2 around 952 GHz. Here, most of the HFS components are resolved and the intensity of the absorption lines is well above the 3σ noise level threshold.

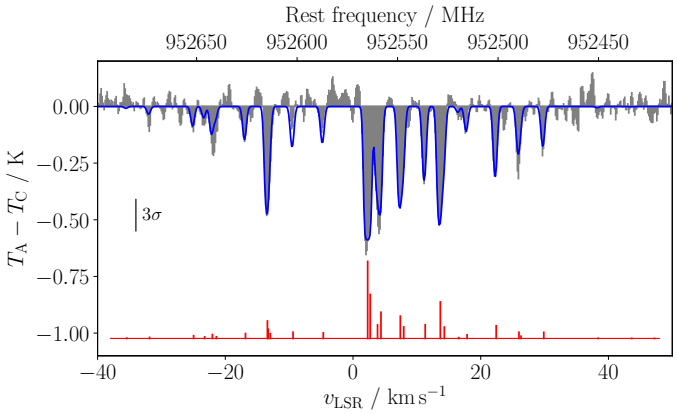

Fig. 1. Spectrum of the $J = \frac{3}{2} - \frac{1}{2}$ component of the $N_{Ka,Kc} = 1_{1,1} - 0_{0,0}$ *o*-NH_2 transition around 952 GHz observed towards IRAS 16293-2422. The filled gray histograms show the observed spectra, while the blue trace is our HFS fit. The red sticks represent the position of the HFS components assuming LTE intensities.

The resulting model of the full HFS (plotted with the solid blue line in Fig. 1) has been computed using a custom `Python3` code which exploits a similar approach to that of the `HFS` method implemented in CLASS. Differently from the latter, our code uses the column density (N) and the excitation temperature ($T_{\rm ex}$) as fit parameters, whereas the total opacity of the transition (τ) is regarded as a derived quantity. To this aim, the routine makes use of the physical line parameters and implements the computation of the rotational partition function for any given $T_{\rm ex}$. The set of the fit parameters also includes the line systemic velocity (v_0) in the local standard of rest, and the full-width half maximum of the lines (FWHM, Δv). Briefly, for a given input the total line

[1] Heterodyne Instrument for the Far-Infrared.
[2] Chemical Herschel surveys of star forming regions.
[3] ESA *Herschel* Science Archive `http://archives.esac.esa.int/hsa/whsa`.
[4] See GILDAS home page at the URL: `http://www.iram.fr/IRAMFR/GILDAS`.

opacity is first calculated through:

$$\tau = \sqrt{\frac{\ln 2}{16\pi^3}} \frac{c^3 A_{ul} g_u N}{\nu^3 Q_{\rm rot}(T_{\rm ex}) \Delta v} \exp\left(\frac{-E_{\rm low}}{k_{\rm B} T_{\rm ex}}\right) \left[1 - \exp\left(\frac{-h\nu_0}{k_{\rm B} T_{\rm ex}}\right)\right], \quad (1)$$

where ν_0 is the rest frequency of the (unsplit) rotational transition, c is the speed of light, $Q_{\rm rot}(T_{\rm ex})$ is the rotational partition function at $T_{\rm ex}$, g_u is the degeneracy of the upper level, A_{ul} is the Einstein coefficient for spontaneous emission, $E_{\rm low}$ is the energy of the lower state, h is the Planck constant, and $k_{\rm B}$ is the Boltzmann constant. Then, assuming the local thermodynamic equilibrium (LTE) approximation and Gaussian profiles, the opacity of the i-th HFS components is computed as $\tau_i = \tau R_i$, where R_i is the corresponding normalised relative intensity. The i-th component opacity at each velocity channel is then given by:

$$\tau_i(v) = \tau_i \exp\left[-4 \ln 2 \left(\frac{v - v_{0,i}}{\Delta v}\right)^2\right], \quad (2)$$

where $v_{0,i}$ is the corresponding velocity position expressed as an offset with respect to the systemic velocity v_0. Finally, the continuum-subtracted antenna temperature at a given velocity channel v is modeled as

$$T_{\rm ant}(v) = [J_\nu(T_{\rm ex}) - J_\nu(T_{\rm CMB}) - T_{\rm C}]\left(1 - {\rm e}^{-\sum_i \tau_i(v)}\right), \quad (3)$$

where $J_\nu(T)$ is the Rayleigh–Jeans radiation temperature, $T_{\rm C}$ is the temperature of the continuum and $T_{\rm CMB}$ is the cosmic background temperature. These data are compared to the continuum-subtracted observed antenna temperatures, $T_{\rm A} - T_{\rm C}$, in a non-linear least-squares fashion to determine the best fit values of N, $T_{\rm ex}$, Δv, and v_0. Whenever possible, all four parameters have been adjusted during the analysis. This sometimes produced strong correlation between them, specially when fitting weak features (e.g., those of ND_2), for which the relative intensities of the observed HFS components are poorly constrained because of the low signal-to-noise ratio (S/N). In these cases, suitable assumption for $T_{\rm ex}$ and Δv had to be used and the corresponding parameters were kept fixed in the least-squares fit. The single-sideband continuum temperature $T_{\rm C}$, inserted in the radiative transfer equality of Eq. (3), has been estimated using the linear formula given by Hily-Blant et al. (2010), $T_{\rm C}/[{\rm K}] = 1.10\,\nu - 0.42$, with ν expressed in THz.

The spectroscopic data for NH_2, NHD, and ND_2 have been taken from the most recent laboratory studies (Martin-Drumel et al. 2014; Bizzocchi et al. 2020; Melosso et al. 2017), and the $Q_{\rm rot}$ values used in Eq. (1) have been computed at any given temperature by cubic interpolation on a grid of finely spaced entries spanning the 2.7–19 K interval. These were obtained by direct summation on all rotational levels through the SPCAT spectral tool (Pickett 1991), with the *ortho* and *para* species of the symmetric isotopologues NH_2 and ND_2 treated separately. A brief explanation of the energy levels structure of NHD and ND_2 is given in Appendix A, while the complete list of HFS components used for the analysis of each transition is reported in Appendix C. The partition function values of both species computed at temperatures between 2.725 and 300 K are given in Appendix B.

4. Results

The line parameters obtained from the analysis of the observed transitions of NH_2, NHD, and ND_2 are collected in Table 1. In the first two rows, the results obtained for the fine-structure line of o-NH_2 detected previously by Hily-Blant et al. (2010) are reported. Our fitted N and $T_{\rm ex}$ values compare very well with those obtained from the CLASS HFS method employed in that study. Our weighted average of the column density is $(5.4 \pm 0.4) \times 10^{13}$ cm^{-2}, which is consistent within the uncertainty with the value $(4.4 \pm 0.7) \times 10^{13}$ cm^{-2} obtained previously. The excitation temperatures determined for the two components are 1σ coincident (8.44 ± 0.12 K the average), and are also close to the ones obtained by Hily-Blant et al. (2010) (8.5 K for the $J = \frac{3}{2} - \frac{1}{2}$ and 9.5 K for $J = \frac{1}{2} - \frac{1}{2}$).

In the same spectral survey, we detect for the first time two groups of hyperfine transitions belonging to the singly-deuterated form of amidogen radical, NHD. Figure 2 shows the two fine-structure components of the fundamental $N_{Ka,Kc} = 1_{1,1} \leftarrow 0_{0,0}$ transition of NHD, both observed in absorption around 770 and 776 GHz in the 2b HIFI band.

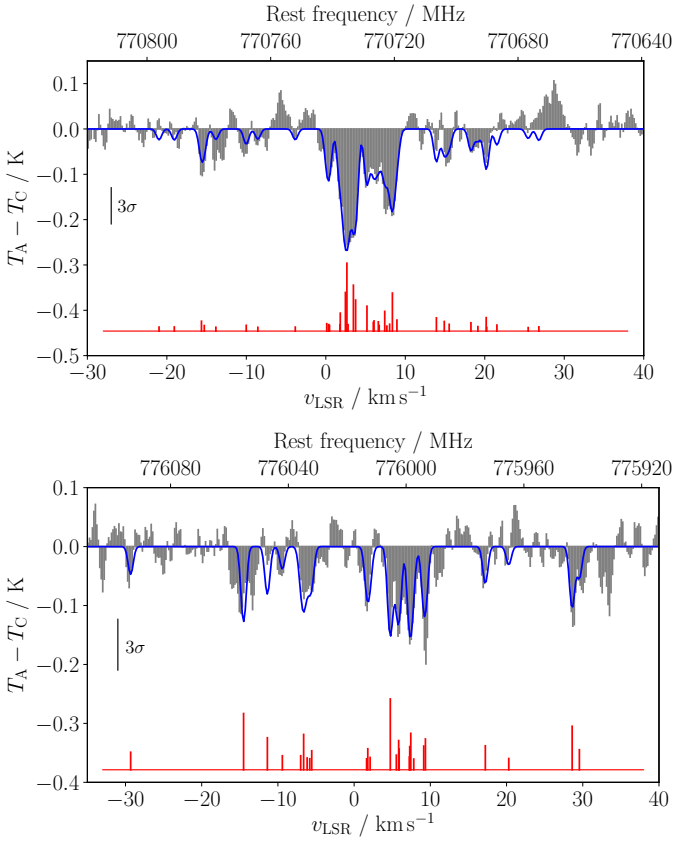

Fig. 2. Spectra of the fine-components of the $N_{Ka,Kc} = 1_{1,1} \leftarrow 0_{0,0}$ NHD transition observed towards IRAS 16293-2422. *Upper panel:* $J = \frac{3}{2} - \frac{1}{2}$ component at *ca.* 770 GHz. *Lower panel:* $J = \frac{1}{2} - \frac{1}{2}$ component at *ca.* 776 GHz. The filled gray histograms show the observed spectra, while the blue trace is our HFS fit. The red sticks represent the position of the HFS components assuming LTE intensities.

Since the $J = \frac{3}{2} - \frac{1}{2}$ fine-structure line is detected at ca. 10σ level, we could adjust all the four parameters in the model. The $J = \frac{1}{2} - \frac{1}{2}$ component is about twice weaker and its detection is only at ca. 5σ level. In this case, the noise prevented to adjust $T_{\rm ex}$ and Δv, which were then fixed at the values obtained for the strongest component of the fine-structure doublet. For NHD, we found an excitation temperature of 7.4 ± 0.1 K, slightly lower than that of NH_2. This small difference is likely to be produced by the bigger *Herschel* beam size in the 2b band ($\sim 27''$) compared to that in the 4a band ($\sim 22''$). Indeed, a larger region is sampled for the NHD lines, and the contribution of the inner

Table 1. Summary of the transitions observed for NH_2, NHD, and ND_2 towards IRAS 16293-2422.

Species	Transition $N_{K_a,Kc}, J$	Frequency [a] [GHz]	HPBW [b] [arcsec]	T_C [K]	T_{ex} [K]	v_{LSR} [km s^{-1}]	Δv [c] [km s^{-1}]	N [10^{13} cm^{-2}]	τ [d]
o-NH_2	$1_{1,1}, \frac{3}{2} - 0_{0,0}, \frac{1}{2}$	952.5722	22.4	0.81	8.6(1)	4.096(9)	0.67(8)	5.3(3)	20.3(13)
	$1_{1,1}, \frac{1}{2} - 0_{0,0}, \frac{1}{2}$	959.5043	22.1	0.82	8.8(3)	4.077(9)	0.66(8)	6.8(9)	13.0(12)
NHD	$1_{1,1}, \frac{3}{2} - 0_{0,0}, \frac{1}{2}$	770.7422	27.5	0.55	7.4(1)	4.19(3)	0.78(11)	4.4(6)	10.3(15)
	$1_{1,1}, \frac{1}{2} - 0_{0,0}, \frac{1}{2}$	776.0177	27.3	0.56	7.4	4.10(3)	0.78	5.0(3)	5.8(5)
p-ND_2	$2_{1,2}, \frac{5}{2} - 1_{0,1}, \frac{3}{2}$	784.9317	27.0	0.57	7.4	4.23(4)	0.78	0.23(1)	2.4(2)
	$2_{1,2}, \frac{3}{2} - 1_{0,1}, \frac{1}{2}$	786.8526	26.9	0.57	7.4	4.31(6)	0.78	0.27(2)	1.5(2)
o-ND_2	$1_{1,1}, \frac{3}{2} - 0_{0,0}, \frac{1}{2}$	527.1808	40.2	0.20	4.5	3.98(7)	0.83	0.66(8)	2.0(3)

Notes. Numbers in parentheses refer to 1σ uncertainties expressed in units of the last quoted digit. [(a)] Rest frequency corresponding to the hypothetically unsplit fine-structure transition. [(b)] Half-power beam width of the observations. [(c)] A conservative uncertainty of 0.25 MHz produced by the HIPE pipeline is summed in quadrature. [(d)] Derived through Eq. (1).

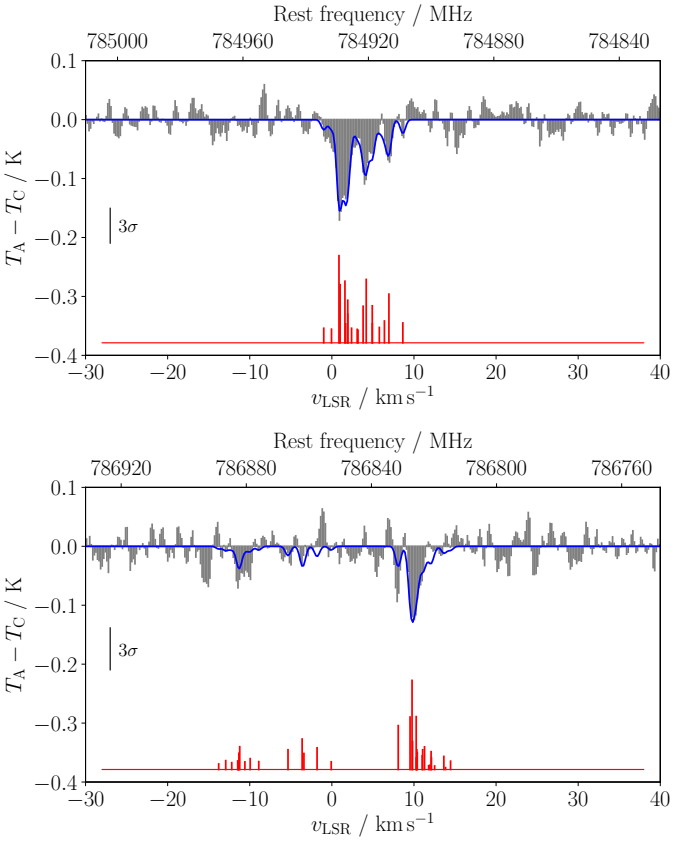

Fig. 3. Spectra of the fine-structure components of the $N_{Ka,Kc} = 2_{1,2} \leftarrow 1_{0,1}$ *p*-ND_2 transition observed towards IRAS 16293-2422. *Upper panel:* $J = \frac{5}{2} - \frac{3}{2}$ component at ca. 785 GHz. *Lower panel:* $J = \frac{3}{2} - \frac{1}{2}$ component at ca. 787 GHz. The filled grey histograms show the observed spectra, while the blue trace is our HFS fit. The red sticks represent the position of the HFS components assuming LTE intensities.

warmer gas is expected to be slightly smaller. The average value of the column density is $N = (4.7 \pm 0.7) \times 10^{13}$ cm^{-2}.

Compared to the parent isotopologue, the doubly deuterated form of amidogen has a denser spectrum in the sub-millimeter region, thus both the $N_{Ka,Kc} = 1_{1,1} \leftarrow 0_{0,0}$ and $N_{Ka,Kc} = 2_{1,2} \leftarrow 1_{0,1}$ rotational lines fall within the coverage of the CHESS spectral survey. A clear detection has been obtained in the 2b band for both $J = \frac{5}{2} - \frac{3}{2}$ and $J = \frac{3}{2} - \frac{1}{2}$ fine-structure components of the $N_{Ka,Kc} = 2_{1,2} \leftarrow 1_{0,1}$ transitions of the *para* species. They are shown in Fig. 3. The $N_{Ka,Kc} = 1_{1,1} \leftarrow 0_{0,0}$, $J = \frac{3}{2} - \frac{1}{2}$ of the *ortho* species, illustrated in Fig. 4, is located at 527 GHz.

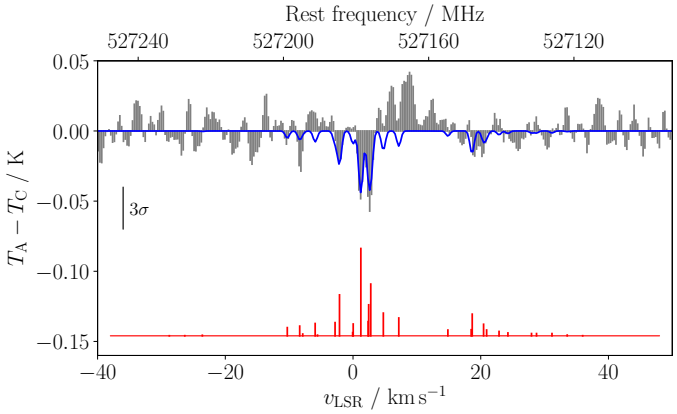

Fig. 4. Spectrum of the $J = \frac{3}{2} - \frac{1}{2}$ component of the $N_{Ka,Kc} = 1_{1,1} - 0_{0,0}$ *o*-ND_2 transition around 527 GHz observed towards IRAS 16293-2422. The filled gray histograms show the observed spectra, while the blue trace is our HFS fit. The red sticks represent the position of the HFS components assuming LTE intensities.

In this spectral region, covered by the HIFI 1a band, the continuum emission of the source is only 200 mK; hence, the resulting absorption feature is rather faint and the detection is only marginal, reaching at most 5σ. The other fine-structure component (intrinsically less intense) is just below the noise level and not detected. Given the weakness of all the three components observed for ND_2, their analysis had to be carried out adopting suitable assumptions for T_{ex} and Δv, as these parameters could not be set free in the least-squares fits. Given the similarity of the beam size ($\sim 27''$), for the *p*-ND_2 $N_{Ka,Kc} = 2_{1,2} \leftarrow 1_{0,1}$ lines we have assumed the same excitation temperature determined for NHD. A smaller value is expected to hold for the *o*-ND_2 $N_{Ka,Kc} = 1_{1,1} \leftarrow 0_{0,0}$ line, as the *Herschel* beam HPBW at this frequency is as broad as $40''$, thus sampling a comparatively large volume of cold gas. For this transition we have fixed $T_{ex} = 4.5$ K, a value determined for ND in the same source (Bacmann et al. 2010) through the analysis of its $N = 1 - 0$ fine-

structure doublet centered at 534 GHz. In fact, this value allows for a satisfactory fit of the absorption *o*-ND_2 feature, whereas for higher excitation temperatures (e.g., already at 5.5 K) the LTE model predicts the line to be observable in emission. Constraints for the FWHM line width Δv have been derived from the values determined for NH_2 after deconvolution from the WBS spectrometer resolution (1.1 MHz). The column densities derived for *p*-ND_2 using two components are consistent within 2σ and the weighted average value is $N = (0.241 \pm 0.014) \times 10^{13}\,\mathrm{cm}^{-2}$. The observed *ortho*-to-*para* ratio is 2.7 ± 0.4. By considering (i) the energy difference of $10.77\,\mathrm{cm}^{-1}$ ($E/k \approx 15.5$ K) between the lowest *para* and *ortho* rotational levels, and (ii) the spin statistical weights, this ratio corresponds to an equilibrium temperature of 9 ± 1 K. Due to the different beam sizes used to observe the $N_{Ka,Kc} = 1_{1,1} \leftarrow 0_{0,0}$, and $2_{1,2} \leftarrow 1_{0,1}$ transitions, the *p*-ND_2 is preferentially sampled in the inner warmer region; therefore, this value is likely to be slightly overestimated.

For the same reason, the evaluation of the abundance ratios between amidogen isotopologues requires some careful considerations. From the averaged N values we obtained $[NHD]/[NH_2] = 0.87 \pm 0.14$, hinting to a very high deuteration level for amidogen, lying in the 70-100% range. We consider this results as robust. The HPBW of the observations differs by only 25%, thus the source area sampled by the antenna is similar for both NHD and NH_2 lines. Furthermore, the energy difference between *ortho* and *para* species of NH_2 is $21.11\,\mathrm{cm}^{-1}$ ($E/k_\mathrm{B} \approx 30.4$ K), and the contribution of the unobserved *p*-NH_2 is expected to be less than 5% at 10 K. Finally, since the used transitions have their lower level located at "zero" energy, the product of two exponential terms in Eq. (1) tends to 1 for small $h\nu_0/k_\mathrm{B}T_\mathrm{ex}$, and the relation between N and τ depends only mildly on the temperature. Hence, the retrieved column density values are not much affected by the inaccuracies in the corresponding T_ex determination.

The derivation of sound values of the isotopic ratios involving ND_2 is less straightforward, as various approaches can be adopted to estimate the overall ND_2 column density from the available observational results. By assuming that the two spin species are in thermal equilibrium, total N values of $0.70 \times 10^{13}\,\mathrm{cm}^{-2}$ and $0.98 \times 10^{13}\,\mathrm{cm}^{-2}$ can be obtained from the *o*-ND_2 and *p*-ND_2 results, respectively. A direct sum of the *ortho* and *para* column density with no assumptions gives instead $0.90 \times 10^{13}\,\mathrm{cm}^{-2}$. Based on the resulting 30% discrepancies, we conservatively quote $N = (0.9 \pm 0.3) \times 10^{13}\,\mathrm{cm}^{-2}$ as the total column density of ND_2. This yields $[ND_2]/[NHD] = 0.19 \pm 0.07$ and $[ND_2]/[NH_2] = 0.17 \pm 0.06$, that is, deuteration levels in the 10–30% range. The amidogen D/H ratio measured in the low-mass protostar IRAS16293 is very high and is comparable to the one derived for the related species imidogen ([ND]/[NH]= 30 − 70%, Bacmann et al. 2010), while ammonia shows a lower level ($[NH_2D]/[NH_3] \sim$ 10%, van Dishoeck et al. 1995). The ND_2 species is very abundant, yielding a remarkably high deuteration ratio, even higher than the one found for methanol ($[CHD_2OH]/[CH_3OH]$= 6%, Parise et al. 2004), a species for which the triply deuterated species was also detected in this source.

5. Chemical simulation

A steady-state model of cold and CO-depleted clouds was published by Roueff et al. (2005), but their predictions on deuterium enhancement, i.e., 10% for NHD and below 1% for ND_2, are significantly underestimated with respect to our findings, which are 87% and 18% for NHD and ND_2, respectively.

In an effort to reproduce the observed tendencies of the D/H and spin-state abundance ratios, we have carried out new chemical simulations of (deuterated) amidogen using a model of IRAS16293-2422. We followed the approach described in Brünken et al. (2014) and Harju et al. (2017), where more details can be found. Here, we provide only a brief description of the simulations. For the source model we adopted the one used in the above references, where the physical model from Crimier et al. (2010), which represents the protostellar core, was extended with a layer of gas representing the molecular cloud that the protostellar system lies in (with $n(H_2) = 10^4\,\mathrm{cm}^{-3}$ and $T_\mathrm{dust} = T_\mathrm{gas} = 10$ K). The source model is illustrated in Fig. 5. We considered a two-stage model, in which the chemical evolution was first calculated over time t_1 in physical conditions corresponding to the core extension (stage 1), and then the protostellar core model including the low-density extension was run over time t_2 (stage 2) using the initial chemical abundances obtained from the stage 1. We explored a range of t_1 and t_2 values to search for the best fit to the observed column densities.

The simulation results depend on how the chemical reactions related to (deuterated) amidogen formation are assumed to proceed. Here we used our gas-grain chemical code (Sipilä et al. 2019b) and ran a parameter-space exploration, testing the effects of multilayer (three-phase) ice chemistry (Sipilä et al. 2016) and direct proton/deuteron hop (Sipilä et al. 2019a) as opposed to full scrambling in proton-donation reactions (Sipilä et al. 2015) on the various column densities. As an example of the results, Fig. 5 shows a comparison of the beam-convolved modelled and observed column densities and column density ratios using the multi-layer ice model and full scrambling for proton-donation reactions. The chemical model reproduces very well the column density of *o*-NH_2 and the ND_2/NHD ratio, but fails to reproduce the NHD/NH_2 ratio as well as the NHD and (*ortho* and *para*) ND_2 column densities. Other parameter combinations reproduce instead very well the NHD and (*ortho* and *para*) ND_2 column densities, but strongly overpredict the *o*-NH_2 column density. None of the parameter combinations we explored lead to the observed level for the NHD/NH_2 ratio. The chemical model predicts that most of the NHD column originates near the edge of the protostellar core, where the temperature in the source model ($\sim$14 K at the very edge, rising inward; cf. Fig. 5) inhibits NHD production with respect to NH_2. Indeed, a NHD/NH_2 ratio of unity or above can be produced by the chemical model if the gas is sufficiently dense ($n(H_2) \gtrsim 10^5\,\mathrm{cm}^{-3}$) and cold ($T \sim 10$ K), suggesting that our two-phase approach to the core modelling is inadequate for the modelling of amidogen chemistry, and that a substantial amount of time (of the order of 10^6 yr) is required in the pre-stellar phase for the NHD/NH_2 ratio to increase to the observed level. We stress that in the present work, we did not carry out radiative transfer simulations of the amidogen absorption lines, and therefore the comparison of the modelled column densities against the observed ones does not take into account any excitation effects. We will present an in-depth comparison of the model versus the observations in an upcoming work, where we will also carry out line simulations.

6. Discussion and conclusions

This work presents the very first detection of both deuterated forms of amidogen radical in the ISM. From the observations, column densities and deuterium fractionation values have been derived allowing for a direct comparison with the predictions obtained from chemical networks. We have run a parameter-space exploration using our gas-grain chemical code,

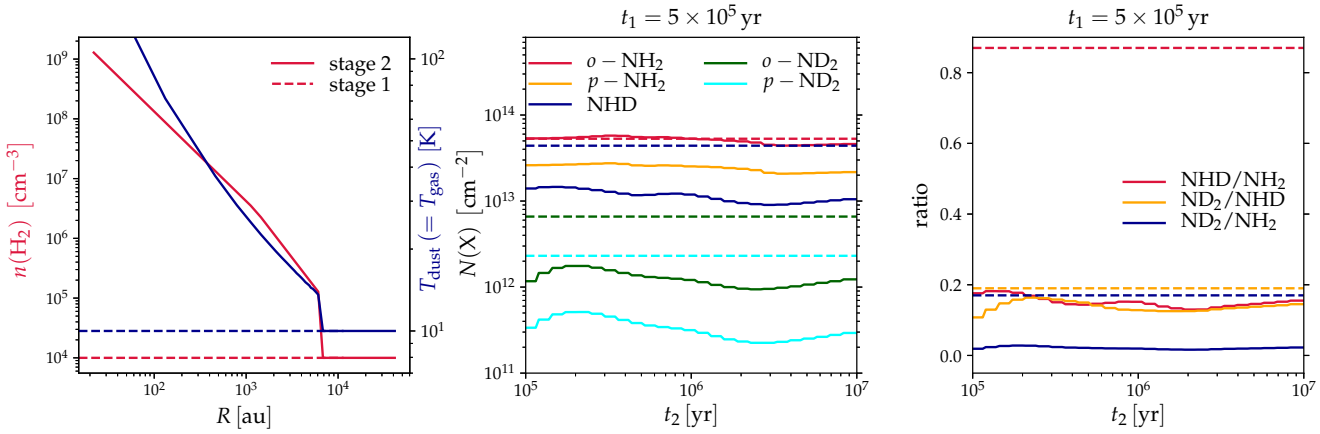

Fig. 5. *Left panel:* Density (red) and temperature (blue) structure in the IRAS16293 source model in stages 1 and 2 (see Sect. 5 for details). *Middle panel:* Modelled beam-convolved molecular column densities (solid lines, labeled in the plot) as functions of time in stage 2. Dashed lines represent the observed values, omitting error bars for clarity. *Right panel:* Modelled D/H ratios (solid lines, labeled in the plot) as functions of time in stage 2. Here, the NH_2 and ND_2 abundances have been summed over the ortho and para forms. Dashed lines represent the observed values, for which the error bars have again been omitted.

implementing a two-stage approach to the dynamical evolution of the source. The observed abundances of all NH_2, NHD, and ND_2 isotopic variants could not be simultaneously reproduced with a single set of modelling parameters, thus indicating that the two-stage approach to the core modelling is inadequate for simulating amidogen isotopic chemistry. More insights on this topic would come from additional observations of deuterated amidogen isotopologues. They are, however, partially hampered by the atmospheric opacity. In fact, The most intense transition of NHD, located at 770 GHz, is not accessible with the ground-based facilities because of nearby strong water absorption lines. Hence, NHD observations can rely mainly on the *a*-type $N_{Ka,Kc} = 1_{0,1} \leftarrow 0_{0,0}$ transition around 413 GHz. Luckily, spectral coverage at this frequency is supported by the ALMA 8 Band and the new nFLASH receiver of APEX. As for ND_2, the transitions detected in this work fall in spectral windows accessible either with the incoming band 1 of the 4GREAT receiver on board SOFIA (490–635 GHz) or ALMA 10 Band (787–950 GHz).

The conclusions of the present work can be summarized as follows:

1. Thanks to the recently obtained laboratory data, two deuterated forms of amidogen radical, namely NHD and ND_2, have been identified for the first time in the ISM. The analysis of hyperfine resolved transitions, observed in absorption against the continuum of the Class 0 protostar IRAS 16293-2422, allowed the accurate determination of column densities and excitation temperatures.
2. The deuterium fractionation of amidogen results to be 70-100% for NHD and 10–30% for ND_2. Our derived values differ significantly, being larger by about one order of magnitude, from those predicted by earlier astrochemical models.
3. The low temperature and the high degree of deuteration observed suggest that amidogen, similarly to other nitrogen-containing species, is less depleted and subsists longer in the gas-phase, thus leading to high abundances of NHD and ND_2.
4. The amidogen D/H and spin-state abundance ratios in IRAS 16293-2422 cannot be reproduced with our gas-grain chemical model unless the pre-stellar stage lasts long, of the order of one million years.
5. ALMA represents the best candidate to perform future observations of NHD and ND_2, not only in IRAS 16293-2422, but also in other sources where deuterated ammonia has been detected. More observations would enable to make a step towards a thorough understanding of ammonia formation and deuteration in the ISM.

Acknowledgements. This study was supported by Bologna University (RFO funds) and by MIUR (Project PRIN 2015: STARS in the CAOS, Grant Number 2015F59J3R). The work at SOLEIL was supported by the Programme National "Physique et Chimie du Milieu Interstellaire" (PCMI) of CNRS/INSU with INC/INP co-funded by CEA and CNES.

References

Bacmann, A., Caux, E., Hily-Blant, P., et al. 2010, A&A, 521, L42
Bacmann, A., Daniel, F., Caselli, P., et al. 2016, A&A, 587, A26
Bizzocchi, L., Melosso, M., Giuliano, B. M., et al. 2020, ApJS, 247
Brown, J., Chalkley, S., & Wayne, F. 1979, Mol. Phys., 38, 1521
Brünken, S., Sipilä, O., Chambers, E. T., et al. 2014, Nature, 516, 219
Butner, H., Charnley, S., Ceccarelli, C., et al. 2007, ApJL, 659, L137
Caselli, P. & Ceccarelli, C. 2012, A&A Rev., 20, 56
Ceccarelli, C., Bacmann, A., Boogert, A., et al. 2010, A&A, 521, L22
Ceccarelli, C., Caselli, P., Bockelée-Morvan, D., et al. 2014, Protostars and Planets VI, 859
Ceccarelli, C., Caselli, P., Herbst, E., Tielens, A. G. G. M., & Caux, E. 2007, in Protostars and Planets V, ed. B. Reipurth, D. Jewitt, & K. Keil, 47
Ceccarelli, C., Castets, A., Loinard, L., Caux, E., & Tielens, A. 1998, A&A, 338, L43
Comito, C. & Schilke, P. 2002, A&A, 395, 357
Crimier, N., Ceccarelli, C., Maret, S., et al. 2010, A&A, 519, A65
de Graauw, T., Helmich, F. P., Phillips, T. G., et al. 2010, A&A, 518, L6
Fayolle, E. C., Öberg, K. I., Jørgensen, J. K., et al. 2017, Nat. Astron., 1, 703
Harju, J., Sipilä, O., Brünken, S., et al. 2017, ApJ, 840, 63
Hily-Blant, P., Maret, S., Bacmann, A., et al. 2010, A&A, 521, L52
Jørgensen, J. K., Favre, C., Bisschop, S. E., et al. 2012, ApJL, 757, L4
Kanada, M., Yamamoto, S., & Saito, S. 1991, J. Chem. Phys., 94, 3423
Kobayashi, K., Ozeki, H., Saito, S., Tonooka, M., & Yamamoto, S. 1997, J. Chem. Phys., 107, 9289
Linsky, J. L. 2003, in Solar System History from Isotopic Signatures of Volatile Elements (Springer), 49–60
Loinard, L., Castets, A., Ceccarelli, C., Caux, E., & Tielens, A. 2001, ApJL, 552, L163
Martin-Drumel, M. A., Pirali, O., & Vervloet, M. 2014, JPCA, 118, 1331
Melosso, M., Bizzocchi, L., Tamassia, F., et al. 2019a, PCCP, 21, 3564
Melosso, M., Conversazioni, B., Degli Esposti, C., et al. 2019b, JQSRT, 222, 186
Melosso, M., Degli Esposti, C., & Dore, L. 2017, ApJS, 233
Melosso, M., Dore, L., Gauss, J., & Puzzarini, C. 2020, J. Mol. Spectrosc.

Ott, S. 2010, in ASP Conf. Ser., Vol. 434, Astronomical Data Analysis Software and Systems XIX, 139
Parise, B., Castets, A., Herbst, E., et al. 2004, A&A, 416, 159
Pickett, H. M. 1991, JMS, 148, 371
Roelfsema, P. R., Helmich, F. P., Teyssier, D., et al. 2012, A&A, 537, A17
Roueff, E., Lis, D. C., Van der Tak, F., Gerin, M., & Goldsmith, P. 2005, A&A, 438, 585
Sipilä, O., Caselli, P., & Harju, J. 2019a, A&A, 631, A63
Sipilä, O., Caselli, P., Redaelli, E., Juvela, M., & Bizzocchi, L. 2019b, MNRAS, 487, 1269
Sipilä, O., Caselli, P., & Taquet, V. 2016, A&A, 591, A9
Sipilä, O., Harju, J., Caselli, P., & Schlemmer, S. 2015, A&A, 581, A122
van der Tak, F. F. S., Schilke, P., Müller, H. S. P., et al. 2002, A&A, 388, L53
van Dishoeck, E. F., Blake, G. A., Jansen, D. J., et al. 1995, ApJ, 447, 760
Vastel, C., Phillips, T., Ceccarelli, C., & Pearson, J. 2003, ApJL, 593, L97

Appendix A: Energy levels scheme

Appendix A.1: Singly-deuterated amidogen radical

The manifold of rotational energy levels is very complex in NHD and its spectrum is characterized by many interactions. First, NHD is a light asymmetric rotor far from the prolate limit ($\kappa = -0.66$) whose electric dipole moment lies in the *ab* principal symmetry plane, with components $\mu_a = 0.67$ D and $\mu_b = 1.69$ D (Brown et al. 1979). Because of the large values of the rotational constants, the room temperature spectrum is quite sparse and peaks in the far-infrared (FIR) region.

NHD is an open-shell molecule with a $\tilde{X}\,^2A''$ ground electronic state. Due to the presence of an unpaired electron, the electronic spin ($\mathbf{S} = 1/2$) couples with the rotational angular momentum $\mathbf{N}$, thus splitting each rotational level N_{K_a,K_c} into two fine-structure sub-levels. The fine-structure levels have either $J = N + 1/2$ or $J = N - 1/2$ quantum numbers, with the exception of the $N = 0$ level, for which only the $J = 1/2$ level exists. The total angular momentum $\mathbf{J}$ further couples with each nuclear spin (I_N and $I_D = 1$, $I_H = 1/2$), giving rise to the so-called hyperfine structure (HFS). The angular momentum coupling scheme adopted takes into account the magnitude of the interaction (from strongest to weakest):

$$\mathbf{J} = \mathbf{N} + \mathbf{S}\,, \tag{A.1a}$$
$$\mathbf{F}_1 = \mathbf{J} + \mathbf{I}_N\,, \tag{A.1b}$$
$$\mathbf{F}_2 = \mathbf{F}_1 + \mathbf{I}_H\,, \tag{A.1c}$$
$$\mathbf{F} = \mathbf{F}_2 + \mathbf{I}_D\,. \tag{A.1d}$$

A more detailed accounts of the NHD spectroscopy can be found in Bizzocchi et al. (2020).

Appendix A.2: Doubly-deuterated amidogen radical

The higher symmetry of ND_2 with respect to NHD requires additional considerations in the description of the energy levels manifold. ND_2 belongs to the C_{2v} symmetry point group and a π-rotation along the *b* axis exchanges the two identical deuterium nuclei. Since deuterium is a boson, the total wave-function of ND_2 must be symmetric upon the permutation of the two particles. Given that the electronic ground state is antisymmetric ($\tilde{X}\,^2B_1$) and the vibrational ground state is symmetric, deuterium nuclear spin functions ($I_{D,tot} = I_{D_1} + I_{D_2}$) can only combine with rotational levels of opposite symmetry. That is, symmetric rotational levels ($K_a + K_c$ = even) combine with antisymmetric deuterium spin functions, with $I_{D,tot} = 1$ (*ortho* states), while antisymmetric rotational levels ($K_a + K_c$ = odd) combine with the spin functions $I_{D,tot} = 0, 2$ (*para* states). Only transitions within the states are allowed by the permanent electric dipole moment of ND_2 ($\mu_b = 1.82(5)$ D Brown et al. 1979). At low temperature, given the energy difference of 15.5 K between the *ortho* and *para* states, *o*-ND_2 and *p*-ND_2 should be considered as different species.

The network of fine and hyperfine interactions in ND_2 is analogous to that described earlier for NHD, while the coupling scheme of angular momentum changes as follows:

$$\mathbf{F}_1 = \mathbf{J} + \mathbf{I}_N\,, \tag{A.2a}$$
$$\mathbf{F} = \mathbf{F}_1 + \mathbf{I}_{D,tot}\,. \tag{A.2b}$$

A detailed account of the spectroscopic features of ND_2 can be found in Melosso et al. (2017).

Appendix B: Partition function values

The spectroscopic parameters from Bizzocchi et al. (2020) and Melosso et al. (2017) have been input in the SPCAT subroutine (Pickett 1991) to evaluate the rotational partition function of NHD and ND_2, respectively. All the energy levels up to $J = 20$ and $K_a = 15$ have been considered. The temperature-dependence of Q_{rot} has been computed analytically for both species at temperatures between 2.725 and 300 K. These values are given in Table B.1.

Table B.1. Rotational partition function values of NHD and ND_2 computed at different temperatures.

Temperature (K)	NHD	ND_2
300.000	6420.8713	7580.4217
225.000	4176.0818	4927.1928
150.000	2283.1782	2689.7500
75.000	820.8872	962.6221
37.500	301.1282	349.7845
18.750	115.5024	130.1662
9.375	52.9533	48.8603
5.000	38.1321	23.5653
2.725	36.0453	18.3627

Appendix C: List of the used HFS components

Tables C.1–C.5 list the rest frequencies of the observed hyperfine components of NHD and ND_2. The LTE intensities (computed at 300 K and labeled LGINT in the tables) and the HFS quantum numbers are also given. Spectral predictions are based on the spectroscopic studies reported in Melosso et al. (2017) and in Bizzocchi et al. (2020).

Table C.1. List of HFS components used to reproduce the $J = \frac{3}{2} \leftarrow \frac{1}{2}$, $N_{Ka,Kc} = 1_{1,1} \leftarrow 0_{0,0}$ transition of NHD.

Frequency	LGINT	Up. state			Lo. state		
(MHz)	(nm^2 MHz)	F'_1	F'_2	F'	F_1	F_2	F
770684.033	-3.5757	0.5	0	1	1.5	1	1
770697.605	-3.4229	1.5	1	2	1.5	1	1
770701.070	-3.0725	1.5	1	2	1.5	1	2
770703.764	-3.5532	1.5	1	0	1.5	1	1
770706.007	-3.2813	1.5	1	1	1.5	1	2
770713.045	-3.3739	1.5	2	1	1.5	2	1
770714.635	-3.2184	1.5	2	2	1.5	2	2
770717.184	-3.0809	1.5	2	3	1.5	2	3
770729.939	-3.1592	0.5	1	2	0.5	1	2
770731.407	-2.6209	2.5	2	3	1.5	1	2
770732.303	-3.3683	0.5	1	1	0.5	1	1
770733.192	-3.5106	0.5	1	1	0.5	1	0
770733.891	-2.9068	2.5	2	2	1.5	1	1
770735.685	-3.4570	0.5	1	0	0.5	1	1
770735.961	-3.2356	2.5	2	1	1.5	1	0
770737.355	-3.1949	2.5	2	2	1.5	1	2
770737.593	-3.2680	2.5	2	1	1.5	1	1
770739.631	-2.8049	0.5	1	2	0.5	0	1
770743.306	-2.7096	2.5	3	2	1.5	2	1
770744.024	-2.5392	2.5	3	3	1.5	2	2
770745.755	-3.3952	0.5	1	1	0.5	0	1
770746.127	-2.3691	2.5	3	4	1.5	2	3
770746.604	-2.6141	1.5	2	3	0.5	1	2
770748.263	-2.9477	1.5	2	2	0.5	1	1
770748.379	-3.4022	2.5	3	2	1.5	2	2
770751.746	-3.4616	1.5	2	1	0.5	1	1
770751.990	-3.3905	2.5	3	3	1.5	2	3
770752.022	-3.4349	1.5	2	2	0.5	1	2
770752.634	-3.3344	1.5	2	1	0.5	1	0
770762.836	-3.6026	1.5	1	2	1.5	2	3
770778.684	-3.4439	0.5	0	1	0.5	1	2
770792.256	-3.4614	1.5	1	2	0.5	1	2
770793.173	-3.2079	2.5	2	3	1.5	2	3
770801.949	-3.5909	1.5	1	2	0.5	0	1
770806.886	-3.6006	1.5	1	1	0.5	0	1

Table C.2. List of HFS components used to reproduce the $J = \frac{1}{2} \leftarrow \frac{1}{2}$, $N_{Ka,Kc} = 1_{1,1} \leftarrow 0_{0,0}$ transition of NHD.

Frequency	LGINT	Up. state			Lo. state		
(MHz)	(nm^2 MHz)	F'_1	F'_2	F'	F_1	F_2	F
775951.7799	-3.3743	1.5	2	2	1.5	1	1
775954.2373	-3.0381	1.5	2	3	1.5	1	2
775983.7269	-3.2975	1.5	1	2	1.5	2	3
776004.0628	-3.1888	0.5	1	2	1.5	1	2
776004.6459	-3.3020	1.5	2	1	1.5	2	1
776009.0444	-3.1157	1.5	2	2	1.5	2	2
776009.3879	-3.3118	1.5	1	2	0.5	1	1
776009.5205	-3.5730	0.5	0	1	1.5	1	1
776012.9847	-3.3589	0.5	0	1	1.5	1	2
776013.1471	-3.2111	1.5	1	2	0.5	1	2
776013.9374	-3.5115	1.5	1	1	0.5	1	2
776016.0039	-2.8268	1.5	2	3	1.5	2	3
776022.8395	-3.5879	1.5	1	2	0.5	0	1
776023.6298	-3.3538	1.5	1	1	0.5	0	1
776042.6716	-3.3983	1.5	2	2	0.5	1	1
776044.2348	-3.6053	1.5	2	1	0.5	1	0
776045.4241	-3.1291	1.5	2	3	0.5	1	2
776046.4309	-3.5307	1.5	2	2	0.5	1	2
776052.6624	-3.5309	0.5	1	0	1.5	2	1
776057.7495	-3.1714	0.5	1	1	1.5	2	2
776065.8293	-2.9268	0.5	1	2	1.5	2	3
776104.1715	-3.4331	0.5	0	1	0.5	1	2

Table C.3. List of HFS components used to reproduce the $J = \frac{3}{2} \leftarrow \frac{1}{2}$, $N_{Ka,Kc} = 1_{1,1} \leftarrow 0_{0,0}$ transition of ND_2.

Frequency	LGINT	Up. state			Lo. state		
(MHz)	(nm^2 MHz)	F'_1	$I'_{\mathrm{D,tot}}$	F'	F_1	$I_{\mathrm{D,tot}}$	F
527133.0435	-4.2749	0.5	1	0.5	1.5	1	0.5
527137.3007	-4.2731	0.5	1	0.5	1.5	1	1.5
527138.6811	-4.2681	0.5	1	1.5	1.5	1	2.5
527145.1770	-4.1674	1.5	1	2.5	1.5	1	1.5
527147.6220	-3.9877	1.5	1	1.5	1.5	1	0.5
527151.0397	-3.8630	1.5	1	0.5	1.5	1	0.5
527151.8792	-3.5628	1.5	1	1.5	1.5	1	1.5
527155.0073	-3.2897	1.5	1	2.5	1.5	1	2.5
527155.2969	-3.8423	1.5	1	0.5	1.5	1	1.5
527161.7095	-3.8657	1.5	1	1.5	1.5	1	2.5
527175.2302	-3.3744	0.5	1	1.5	0.5	1	1.5
527179.4875	-3.2692	0.5	1	1.5	0.5	1	0.5
527182.9457	-2.9117	2.5	1	2.5	1.5	1	1.5
527183.5235	-3.1343	2.5	1	1.5	1.5	1	0.5
527183.6802	-3.4747	0.5	1	0.5	0.5	1	1.5
527185.6745	-2.6845	2.5	1	3.5	1.5	1	2.5
527187.7807	-3.5532	2.5	1	1.5	1.5	1	1.5
527187.9375	-4.1230	0.5	1	0.5	0.5	1	0.5
527191.5565	-3.0134	1.5	1	2.5	0.5	1	1.5
527192.7760	-3.5051	2.5	1	2.5	1.5	1	2.5
527198.2587	-3.5357	1.5	1	1.5	0.5	1	1.5
527201.6764	-4.3765	1.5	1	0.5	0.5	1	1.5
527202.5160	-3.6385	1.5	1	1.5	0.5	1	0.5
527205.9337	-3.7120	1.5	1	0.5	0.5	1	0.5

Table C.4. List of HFS components used to reproduce the $J = \frac{5}{2} \leftarrow \frac{3}{2}$, $N_{Ka,Kc} = 2_{1,2} \leftarrow 1_{0,1}$ transition of ND_2.

Frequency	LGINT	Up. state			Lo. state		
(MHz)	(nm^2 MHz)	F'_1	$I'_{\mathrm{D,tot}}$	F'	F_1	$I_{\mathrm{D,tot}}$	F
784901.6100	-3.3624	2.5	2	3.5	2.5	2	3.5
784901.8686	-3.3381	2.5	0	2.5	2.5	0	2.5
784903.2122	-3.2352	2.5	2	4.5	2.5	2	4.5
784906.4925	-3.4213	1.5	2	2.5	1.5	2	2.5
784906.9759	-3.2482	1.5	2	3.5	1.5	2	3.5
784907.7212	-3.3377	1.5	0	1.5	1.5	0	1.5
784912.0082	-3.4046	1.5	2	0.5	1.5	2	1.5
784913.9865	-3.4905	1.5	2	1.5	1.5	2	2.5
784920.0864	-2.8823	1.5	2	2.5	0.5	2	1.5
784924.5270	-2.4925	1.5	2	3.5	0.5	2	2.5
784925.9631	-2.8414	1.5	0	1.5	0.5	0	0.5
784927.5805	-2.9946	1.5	2	1.5	0.5	2	1.5
784929.8205	-2.9028	2.5	2	2.5	1.5	2	1.5
784929.8382	-2.6114	2.5	2	3.5	1.5	2	2.5
784931.7629	-2.3779	2.5	2	4.5	1.5	2	3.5
784932.0249	-3.2870	2.5	2	1.5	1.5	2	0.5
784932.2158	-3.3227	1.5	2	0.5	0.5	2	1.5
784932.7588	-2.6164	2.5	0	2.5	1.5	0	1.5
784934.3875	-3.0821	2.5	2	1.5	1.5	2	1.5
784934.6498	-3.0523	1.5	2	2.5	0.5	2	2.5
784934.6762	-3.2289	2.5	2	0.5	1.5	2	0.5
784936.4341	-3.0168	2.5	2	2.5	1.5	2	2.5
784937.6522	-2.5509	3.5	2	3.5	2.5	2	2.5
784937.6570	-2.7232	3.5	2	2.5	2.5	2	1.5
784938.3512	-2.9047	3.5	2	1.5	2.5	2	0.5
784938.5498	-2.3902	3.5	2	4.5	2.5	2	3.5
784940.0965	-2.4157	3.5	0	3.5	2.5	0	2.5
784940.4444	-3.1259	2.5	2	3.5	1.5	2	3.5
784940.4531	-2.2396	3.5	2	5.5	2.5	2	4.5
784941.3117	-3.2175	3.5	2	1.5	2.5	2	1.5
784942.8337	-3.0461	3.5	2	2.5	2.5	2	2.5
784945.3078	-3.0176	3.5	2	3.5	2.5	2	3.5
784948.8334	-3.1526	3.5	2	4.5	2.5	2	4.5

Table C.5. List of HFS components used to reproduce the $J = \frac{3}{2} \leftarrow \frac{1}{2}$, $N_{Ka,Kc} = 2_{1,2} \leftarrow 1_{0,1}$ transition of ND_2.

Frequency	LGINT	Up. state			Lo. state		
(MHz)	(nm^2 MHz)	F'_1	$I'_{D,tot}$	F'	F_1	$I_{D,tot}$	F
786826.0110	-3.4286	1.5	2	0.5	0.5	2	1.5
786828.1584	-3.2317	1.5	2	1.5	0.5	2	1.5
786832.1370	-3.2842	1.5	2	2.5	0.5	2	1.5
786832.2338	-3.0963	2.5	2	3.5	1.5	2	3.5
786834.3398	-2.9932	2.5	2	2.5	1.5	2	2.5
786834.9400	-3.0538	2.5	2	1.5	1.5	2	1.5
786835.0841	-3.2113	2.5	2	0.5	1.5	2	0.5
786836.6556	-3.1210	1.5	2	2.5	0.5	2	2.5
786836.7849	-3.0547	1.5	0	1.5	0.5	0	0.5
786836.9956	-3.2843	2.5	2	1.5	1.5	2	0.5
786836.9995	-2.6241	2.5	0	2.5	1.5	0	1.5
786838.1735	-2.9018	2.5	2	2.5	1.5	2	1.5
786838.3241	-2.3974	2.5	2	4.5	1.5	2	3.5
786838.9615	-2.6275	2.5	2	3.5	1.5	2	2.5
786842.7431	-2.7050	1.5	2	3.5	0.5	2	2.5
786864.1688	-3.4603	0.5	2	1.5	0.5	2	1.5
786868.6874	-3.0107	0.5	2	1.5	0.5	2	2.5
786872.8893	-3.1436	0.5	0	0.5	0.5	0	0.5
786873.4617	-2.8638	0.5	2	2.5	0.5	2	1.5
786877.9803	-3.0524	0.5	2	2.5	0.5	2	2.5
786887.3254	-3.4508	1.5	2	2.5	1.5	2	3.5
786890.0744	-3.3125	1.5	2	1.5	1.5	2	2.5
786891.7607	-3.4671	1.5	2	0.5	1.5	2	1.5
786893.4129	-2.9898	1.5	2	3.5	1.5	2	3.5
786893.6763	-3.1369	1.5	0	1.5	1.5	0	1.5
786894.0531	-3.4158	1.5	2	2.5	1.5	2	2.5
786897.8867	-3.4000	1.5	2	2.5	1.5	2	1.5